

ORIGINAL ARTICLE

Open Access



# Dynamic Resistance and Energy Absorption of Sandwich Beam via a Micro-Topology Optimization

Shiqiang Li<sup>1,2</sup>, Yuwei Li<sup>1,2</sup>, Xiaomin Ma<sup>1,2</sup>, Jianguang Fang<sup>3</sup>, Zhifang Liu<sup>1,2</sup> and Zhihua Wang<sup>1,2\*</sup>

## Abstract

The current research of sandwich structures under dynamic loading mainly focus on the response characteristic of structure. The micro-topology of core layers would sufficiently influence the property of sandwich structure. However, the micro deformation and topology mechanism of structural deformation and energy absorption are unclear. In this paper, based on the bi-directional evolutionary structural optimization method and periodic base cell (PBC) technology, a topology optimization frame work is proposed to optimize the core layer of sandwich beams. The objective of the present optimization problem is to maximize shear stiffness of PBC with a volume constraint. The effects of the volume fraction, filter radius, and initial PBC aspect ratio on the micro-topology of the core were discussed. The dynamic response process, core compression, and energy absorption capacity of the sandwich beams under blast impact loading were analyzed by the finite element method. The results demonstrated that the over-pressure action stage was coupled with the core compression stage. Under the same loading and mass per unit area, the sandwich beam with a 20% volume fraction core layer had the best blast resistance. The filter radius has a slight effect on the shear stiffness and blast resistances of the sandwich beams. But increasing the filter radius could slightly improve the bending stiffness. Upon changing the initial PBC aspect ratio, there are three ways for PBC evolution: The first is to change the angle between the adjacent bars, the second is to further form holes in the bars, and the third is to combine the first two ways. However, not all three ways can improve the energy absorption capacity of the structure. Changing the aspect ratio of the PBC arbitrarily may lead to worse results. More studies are necessary for further detailed optimization. This research proposes a new topology sandwich beam structure by micro-topology optimization, which has sufficient shear stiffness. The micro mechanism of structural energy absorption is clarified, it is significant for structural energy absorption design.

**Keywords** Topology optimization, Sandwich beam, Impact loading, Dynamic resistance, Energy absorption, Micro mechanism

## 1 Introduction

Sandwich structures are of wide use in protection engineering owing to their low densities, high specific strengths, and effective energy absorption. The impact energy is dissipated by the macro- and micro-compression and the damage development of core materials during structural collapse. Over the last decade, many core topologies for sandwich panels have emerged, showing structural advantages over monolithic construction for quasi-static loading. These include metallic foams

\*Correspondence:

Zhihua Wang  
wagnzh077@163.com

<sup>1</sup> Institute of Applied Mechanics, Taiyuan University of Technology, Taiyuan 030024, China

<sup>2</sup> Shanxi Key Laboratory of Material Strength and Structural Impact, Taiyuan University of Technology, Taiyuan 030024, China

<sup>3</sup> School of Civil and Environmental Engineering, University of Technology Sydney, Sydney, NSW 2007, Australia



© The Author(s) 2024. **Open Access** This article is licensed under a Creative Commons Attribution 4.0 International License, which permits use, sharing, adaptation, distribution and reproduction in any medium or format, as long as you give appropriate credit to the original author(s) and the source, provide a link to the Creative Commons licence, and indicate if changes were made. The images or other third party material in this article are included in the article's Creative Commons licence, unless indicated otherwise in a credit line to the material. If material is not included in the article's Creative Commons licence and your intended use is not permitted by statutory regulation or exceeds the permitted use, you will need to obtain permission directly from the copyright holder. To view a copy of this licence, visit <http://creativecommons.org/licenses/by/4.0/>.

[1–3], honeycombs [4–7], corrugated cores [8, 9], lattice materials with pyramidal and tetrahedral arrangements [10–13], egg-box structures [14], triply periodic minimal surface (TPMS) structures [15] and cores with negative Poisson's ratios [16–19].

Although the core has several vital functions, such as sound absorption [20–25], it must be stiff enough in the direction perpendicular to the skins, stiff enough to keep the skins nearly flat, and stiff enough in the shear direction to ensure that they remain the correct distance apart and that the skins do not undergo local buckling and slide over each other under a bending load. Because the influence of the material micro-topological configuration on the macroscopic structural properties is complex, there is a lack of material/structure integrated design theory that combines the micro-deformation mechanism with the macroscopic properties. The influence of the load history and structural elastic–plastic response on the structural design variables needs to be considered comprehensively in the optimization process, which involves space–time non-linearity of the load and the nonlinear effects of the material/structure, such as inertial and strain rate effects under impact loading conditions, resulting in a complex objective function and difficulty in sensitivity analysis. Most of the research on these materials and structures focused on performance exploration, application development, and parameter optimization design [26, 27], while the studies on the structural topological design have not been sufficiently in depth. Finally, it is difficult and costly to prepare specially designed porous materials with complex topological configurations. This also leads to separation between the design of porous materials and their sandwich structures under impact loads and the analysis, characterization, and performance evaluation of the dynamic response characteristics. There is no unified design and analysis system, which significantly restricts the development of such materials and structures.

The micro-topological configuration of a cellular material is one of the important factors affecting the macroscopic mechanical behavior of materials and structures. Compared with parameter and shape optimization, topology optimization has a larger design space in a given design domain, and it is a key and popular topic in the field of sandwich structure design [28]. Topology optimization may greatly enhance the performances of materials and structures for many engineering applications. It has been exhaustively studied, and various topology optimization methods have been developed over the past few decades, e.g., the solid isotropic material with penalization (SIMP) method [29], evolutionary structural optimization (ESO) method [30], bi-directional evolutionary structural optimization (BESO) method [31, 32], moving morphable component (MMC) method [33],

feature-drive method [34, 35], level set method [36, 37], independent continuous mapping (ICM) method [38], and feasible domain adjustment topology optimization method [39].

The main idea of topology optimization is to change the material and structural properties by changing the micro-configuration, for example, to increase the structural stiffness by introducing a contact mechanism into the cellular structure [40]. In the process of optimization, it is necessary to consider the effect of the micro-structural properties on the macroscopic structural performance. For a sandwich structure, because the cell size of the core layer is much smaller than the whole structure, the effect of the micro-structural properties of the core layer on the macroscopic structural performance can be determined by homogenization theory [41–43]. However, a large amount of computing resources will be required to calculate the effect of the micro-structure on the performance of the macro-structure directly by using the homogenization method [28]. In addition, the topological configuration obtained based on the homogenization method will contain transition regions, resulting in unclear structures, which is not conducive to manufacturing [43] and cannot reflect the scale effect of representational cells [44]. To solve these problems, the Kriging model was applied by Zhang et al. [28] to improve the calculation efficiency of the homogenization method. Based on homogenization theory, the micro-structure can be assumed to be uniform in the macro scale to meet the manufacturing requirements, and the design variables for the structure and the material micro-structure can be independently defined and integrated into one system. Liu et al. [43] presented a concurrent topology optimization method to simultaneously achieve the optimal structure and material micro-structure for minimum system compliance. Under a simply loaded case where the frames top boundary was downward loaded, Streket et al. [45] employed the SIMP model and found the optimal distribution for a given amount of material in the sandwich-structured composite with minimum compliance. Long et al. [46] proposed a two-scale concurrent topology optimization method for maximizing the frequency of the composite macro-structure. They found that the frequencies of the optimal composites with a specific range of the micro-scale level volume fraction were higher than those of structures made of individual base materials. Li et al. [37] developed a new hierarchical multi-scale formulation to account for both the auxetic behavior of the micro-structure and the stiffness of the macro-structure.

Sandwich structures with core layers formed by effectively combining materials with different properties or

different micro-configurations through topology optimization have better bearing capacities than traditional sandwich structures, but materials and structures exhibit highly nonlinear effects under impact loads. In addition, there is no unified conclusion on whether the optimal topological structure based on quasi-static linear analysis can meet the requirements of impact loads or how to regulate the properties of materials by changing the material composition or micro-structure. Additionally, the optimization of materials and structures under impact loads involves nonlinear factors such as elastic–plastic analysis, large deformation analysis, strain rate effects, and inertial effects, which makes the objective function complex and sensitivity analysis difficult, and the optimization cannot converge in some cases. In some studies, all kinds of nonlinear effects of impact problems were considered first in the process of obtaining a topology optimization design, but the updating rules of the design variables were not obtained through analytical mathematical derivation [47–49], such as the hybrid cellular automata (HCA) method [50]. Park [51] proposed an equivalent static load (ESL) method, which was based on a static load that generated the same displacement field as those in non-linear analysis. The ESL method can be used for linear dynamic response optimization, structural optimization for multi-body dynamical systems, structural optimization for flexible multi-body dynamical systems, nonlinear static response optimization, and nonlinear dynamic response optimization. However, the method is based on the rigid body assumption, and the plastic property of the material cannot be considered [52]. Based on the inertia relief and HCA methods, Yan et al. [53, 54] proposed a hybrid approach for structural topology optimization of crashworthiness. However, the response of the maximum impact loading was only considered in the optimization process, and it was difficult to make a definitive conclusion about whether the structure was beneficial in the large deformation process. Evaluating the dynamic resistance of structures optimized under static conditions is also a very important and effective method of structure design.

For a sandwich structure used for sacrificial cladding, the loading condition is more complex, and the deformation often includes strain rate and stress wave effects. Especially for the metallic materials, researches [55, 56] have been reported that the strain effects have great effects on the mechanical response and failure behaviors. As is well known, the face sheets of the sandwich structure provide a high in-plane stiffness and strength to withstand normal and shear stresses caused by bending moments or in-plane tension. The core layers provide the normal stiffness and strength of the panel to withstand the shear stress generated by compressive and

lateral forces, and they also support the panel [57]. Thus, it is necessary to optimize the sandwich structure based on the mechanical characteristics of the structures and to analyze and verify the structural performance under impact loading conditions.

In the present work, based on the mechanical characteristics of the core layer, which withstands the shear stress and deformation of the sandwich beam, the BESO [41] method was employed to optimize a core composed of a periodic base cell with the maximum shear modulus under a prescribed volume constraint. The dynamic response characteristics and energy absorption ability of the sandwich beam with the maximum shear stiffness core layer under blast impact loading were analyzed by the finite element method.

## 2 Design Optimization Problem

The macroscopic properties of a cellular material can be estimated by the homogenization theory [41] when it is composed of a periodic base cell (PBC) repeatedly and the PBC is smaller than the structure size. The effective elasticity tensor (in index notation)  $E_{ijkl}^H$  of a periodic material can be computed as [58]:

$$E_{ijkl}^H = \frac{1}{|V|} \int_V E_{pqrs} \varepsilon_{ij}^{pq} \varepsilon_{kl}^{rs} dV, \quad (1)$$

where  $|V|$  denotes the total two-dimensional (2D) area or three-dimensional (3D) volume of the PBC domain  $V$ ,  $E_{pqrs}$  is the elasticity tensor (in index notation) of the solid material in index notation, and  $\varepsilon_{ij}^{pq}$ ,  $\varepsilon_{kl}^{rs}$  are the superimposed strain fields, which can be evaluated by solving the base cell equilibrium problem. The detailed description of the homogenization method and the implementation of periodic boundary conditions can be found in Refs. [58, 59].

In order to derive the sensitivity of the macro material elastic property, the local material of an element within the PBC can be treated as isotropic, and its Young's modulus can be interpolated as a function of the element density [41]:

$$E(x_m) = E^1 x_m^p, \quad (2)$$

where  $E^1$  denotes Young's modulus for the solid element,  $p$  is the penalty exponent, and  $x_m$  denotes the relative density of the  $m$ th element.

In 2D optimization problems, the shear modulus of PBC can be expressed as:

$$G = E_{1212}^H. \quad (3)$$

In this paper, only 2D orthotropic cellular material with square symmetry will be considered, the following

relationships exist:  $E_{1111} = E_{2222}$  and  $E_{1122} = E_{2211}$ . Substituting Eq. (2) into Eq. (1), and according to the adjoint method, the sensitivity of the optimization problem can be expressed as the derivative of the homogenized elasticity tensor  $E_{1212}^H$  with respect to the design variable  $x_m$ :

$$\frac{\partial E_{ijkl}^H}{\partial x_m} = \frac{p}{|V|} \int_V x_m^{p-1} E_{pqrs}^1 \varepsilon_{ij}^{pq} \varepsilon_{kl}^{rs} dV, \tag{4}$$

where  $E_{pqrs}^1$  is the elasticity tensor of the solid in index notation.

To maximize the shear modulus, the sensitivity number is:

$$\alpha_m = \frac{1}{p} \frac{\partial G}{\partial x_m}. \tag{5}$$

The mathematical model of the topology optimization with the maximum PBC shear modulus and volume fraction constraint is expressed as:

$$\text{Maximum } G, \tag{6}$$

$$\text{subject to : } \sum_{m=1}^N V_m x_m - V^* = 0, \tag{7}$$

$$x_m = x_{\min} \text{ or } 1, \tag{8}$$

where  $G$  is the shear modulus of the material;  $N$  is the number of microscopic cells;  $V_m$  and  $V^*$  denote the volume of the  $m$ th element and the prescribed volume of the solid phase, respectively; and  $x_m$  is a binary design variable with the value of  $x_{\min}$  (e.g., 0.001 for a void element) and 1 (for a solid element) in the soft-kill BESO method [60].

To circumvent checkerboard patterns and mesh-dependency problems, a mesh-independent filter was employed by averaging the elemental sensitivity number with its neighboring elements based on image-processing techniques [31]. The elemental sensitivity number is given as:

$$\tilde{\alpha}_m = \frac{1}{2} (\hat{\alpha}_{m,n} + \hat{\alpha}_{m,n+1}). \tag{9}$$

In the  $n$ th iteration,

$$\hat{\alpha}_m = \frac{\sum_{j=1}^N w(r_{ij}) \alpha_m}{\sum_{j=1}^M w(r_{ij})}, \tag{10}$$

where  $r_{ij}$  denotes the distance between the center of elements  $i$  and  $j$ .  $w(r_{ij})$  is the weight factor, which is given as:

$$w(r_{ij}) = \begin{cases} r_{\min} - r_{ij}, & \text{for } r_{ij} < r_{\min}, \\ 0, & \text{for } r_{ij} \geq r_{\min}, \end{cases} \tag{11}$$

where  $r_{\min}$  is the filter radius.

The overall procedure for the topology optimization of a microscopic cell based on the BESO method is shown in Figure 1. The material composed of PBCs arranged repeatedly will be used in the following analysis.

Step 1: Define the BESO parameters with objective volume,  $V^*$ , evolutionary ratio  $er=0.02$ , filter radius  $r_{\min}=3$ , and penalty factor  $p = 3$ .

Step 2: Define the orthotropic PBC domain using a finite element mesh. Construct an initial design that assigns four void elements at the center of the design domain, as shown in Figure 2. Young's modulus and Poisson's ratio of the solid material were selected as  $E^1 = 70$  GPa and  $\mu = 0.3$ , respectively.

Step 3: Apply periodic boundaries on the PBC. Conduct finite element analysis (FEA).

Step 4: Based on Eq. (1), calculate the effective elasticity tensor  $E^H$  of the PBC.

Step 5: Calculate and filter the elemental sensitivity numbers  $\hat{\alpha}_m$  according to Eqs. (4), (5), and (9–11).

Step 6: Determine the target volume for the next design, where  $V_n$  is the current volume.

Step 7: Sort the sensitivity numbers and reset the design variables  $x_m$  of all elements.  $\alpha_{th}$  is the threshold of the sensitivity number, which is determined by the target material volume,  $V_{n+1}$ , and the relative ranking of the sensitivity numbers [41]. For example, there were 10000 elements in the design domain and  $\hat{\alpha}_1 > \hat{\alpha}_2 > \dots > \hat{\alpha}_{10000}$ . If  $V_{n+1}$  corresponds to a design with 500 elements, then  $\alpha_{th} = \hat{\alpha}_{500}$ .

Step 8: Repeat Steps 3–7 until both the volume constraint and convergence criterion are satisfied. The convergence criterion is [41]:

$$\frac{\left| \sum_{i=1}^N G_{n-i+1} - G_{n-N-i+1} \right|}{\sum_{i=1}^N G_{n-i+1}} < \tau, \tag{12}$$

where  $G$  is the shear modulus of the micro-structure,  $n$  is the current iteration number,  $\tau$  is an allowable convergence error, and  $N$  is an integer.  $\tau$  and  $N$  were set to be 0.001 and 5, respectively, in the present study.

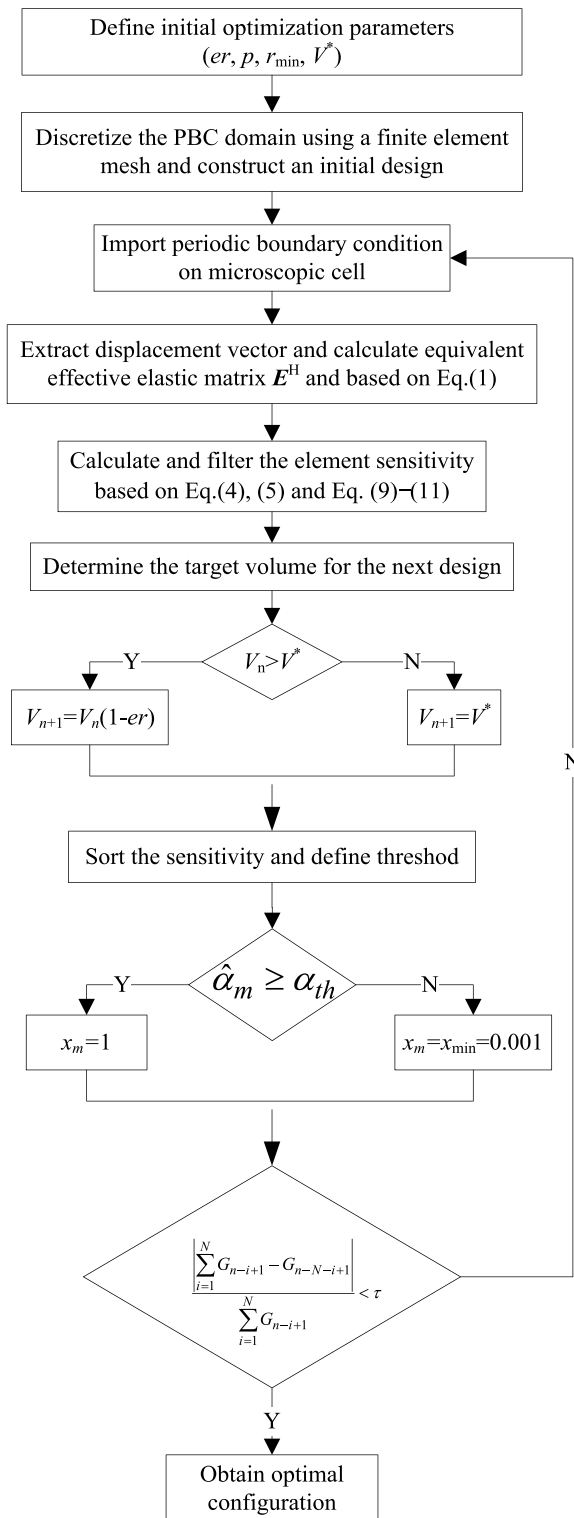


Figure 1 Procedure for micro-structure design

The BESO started from the initial design shown in Figure 2, which was a 5 mm × 5 mm region discretized into 100 × 100 four-node quadrilateral elements.

Convergent solutions were obtained after 138, 92, and 83 iterations when the volume fractions of the solids were 10%, 20%, and 25%, respectively. The final microstructures and effective elasticity matrices are shown in Figure 3(a)–(c), and their shear moduli were 0.024, 0.050, and 0.063. Figure 4 shows the evolution histories of the shear modulus ( $G$ ) and volume fraction ( $V_f$ ). It was also demonstrated that the shear modulus stably converged after the volume constraint was satisfied.

### 3 Geometry Model and Material Properties

#### 3.1 Anatomy of Human Upper-Limb

Imitate the traditional configuration of 2D cellular materials (e.g., honeycombs, corrugated cores), based on the optimization results, the core layer of sandwich beams were modeled by extruding the PBC, as shown in Figure 5. Model V10, Model V20, and Model V25 represent the sandwich beams with cores of 10%, 20%, and 25% volume fractions, respectively. The following parameters were used: The beam width  $B=30$  mm, overall side length  $L=250$  mm, thickness of the core layer  $H_c=30$  mm, thickness of front and back face sheets  $H_f=H_b=1$  mm, and beam thickness  $H = 2H_f + H_c$ . The masses of the beams are shown in Table 1. Solid C3D8R (eight-node linear brick, reduced integration, and hourglass control) brick elements with reduced integration were selected owing to the high capacity to withstand distortion and computational efficiency. Average edge lengths of 0.1 and 0.4 mm were employed to mesh the core layer and face sheets, respectively. Mesh sensitivity studies revealed that further refinement did not significantly improve the accuracy of the calculations.

#### 3.2 Material Properties

The original aluminum-alloy material was simulated by an isotropic and kinematic hardening plasticity model. The following properties were used: The density  $\rho_f = 2700$  kg/m<sup>3</sup>, Young's modulus  $E = 69$  GPa, and Poisson's ratio  $\mu = 0.33$ . Face sheets were made of 1350-H19, whose yield stress  $\sigma_{fY} = 165$  MPa and ultimate tensile strength  $\sigma_{fU} = 185$  MPa. The original aluminum-alloy material of the core layer was 1350-H14, whose yield stress  $\sigma_{cY} = 95$  MPa and ultimate tensile strength  $\sigma_{cU} = 110$  MPa.

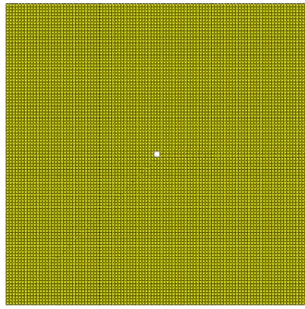


Figure 2 The initial design domain of PBC

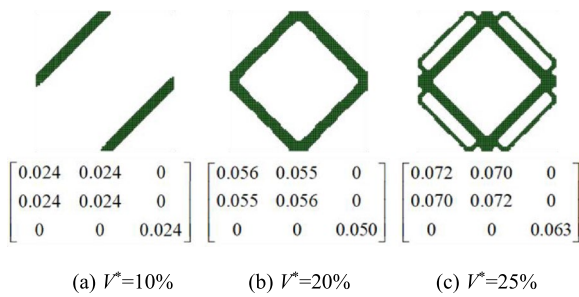


Figure 3 Micro-structures and effective elasticity matrix of orthotropic PBC with maximum shear modulus for various volume constraints

### 3.3 Loading Condition

A near-by explosion condition ( $R_W < a \leq 10R_W$ ) was considered in this study, where  $a$  is the distance of the obstacle surface from the charge center, and  $R_W$  is the radius of a spherical trinitrotoluene (TNT) charge [61]. For the TNT charge blast in air,  $W$  is the charge mass, and  $x$  is the distance of a point on the obstacle surface from the hypocenter, as shown in Figure 6.

In the present study, the blast pressure was determined using the ConWep code in the finite element simulation. This method has also been validated in Refs. [62, 63]. The pressure–time curve  $p(t)$  of a 20 g TNT charge blast at an 80 mm standoff distance is shown in Figure 7. The maximum incident pressure ( $p_i$ ) was 9.313 MPa, the maximum reflection pressure ( $p_r$ ) was 86.394 MPa, the arrival time was 0.18 ms, and the duration was 0.05 ms.

The maximum dynamic impulse  $I$  was calculated as follows:

$$I = \int_0^{\infty} p_r(t) dt. \tag{13}$$

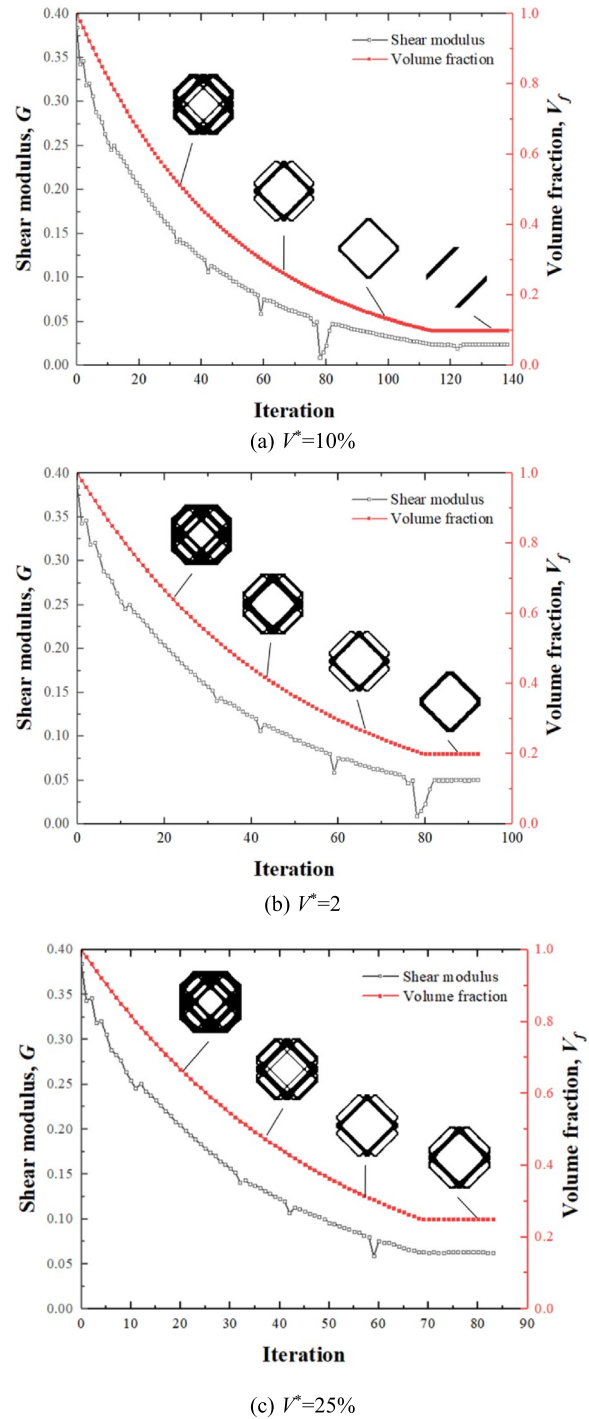


Figure 4 Evolution histories of shear modulus and volume fraction

The normalized impulse is:

$$\bar{I} = \frac{I}{L\sqrt{\sigma_{FY}\rho}}. \tag{14}$$

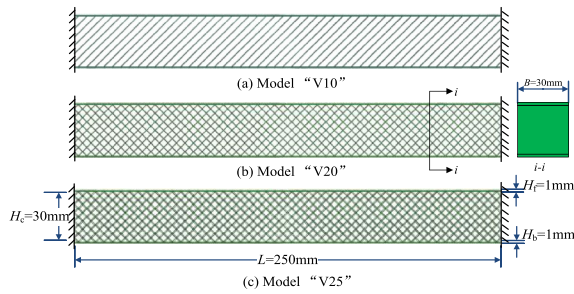


Figure 5 FE model of the sandwich beams

Table 1 Deformation process of V10 mode

$t$ (ms)	Core	Beam deformation mode
0	Initial mode	
0.020	The initial deformation first occurred at the center area of the front face sheet	
0.045	The core layer was compressed progressively. The first lattice layer of the core was densified	
0.15	Due to the asymmetric core layer configuration, the sunken deformation spread to one side	
0.3	The structure presented an asymmetric deformation mode accompanied by a large deformation of the core layer	
0.675	The deflections of the face sheets reached the maximum values. After that, oscillations were observed until the structure came to rest	
1.500	Final deformation mode	

## 4 Results and Discussion

### 4.1 Evaluation of Impact Resistance of the Sandwich Structure

Since personnel or objects shielded from blast attacks are usually behind barriers such as sandwich panels, the mid-span deflection [64–66] of a specimen is considered to be the main response of interest. Because sandwich structures should protect people or objects located on the other side of the explosive, the deflection of the face sheet is another important characterization parameter. The maximum deflection ( $w_{max}$ ) and the residual deflection ( $w_{residual}$ ) can be used as dimensionless parameters to evaluate the blast resistance of structures. The dimensionless parameters are defined as:

$$\bar{w} = \frac{w}{L}, \tag{15}$$

where  $w$  is  $w_{max}$  or  $w_{residual}$ , and  $L$  is the span of the structure.

The energy absorption ratios of the components of the sandwich structures are usually employed to evaluate the performances of structures [67]. Because the energy absorption of the face sheets and core layers can be only obtained from numerical simulations, the energy absorption ratio can be computed as follows:

$$\kappa = \frac{W_c^{int}}{W^{Total}}, \tag{16}$$

where  $W_c^{int}$  is the internal energy of the face sheets or core layers, and  $W^{Total}$  is the total plastic energy of the structure. The specific energy absorption (SEA) is defined

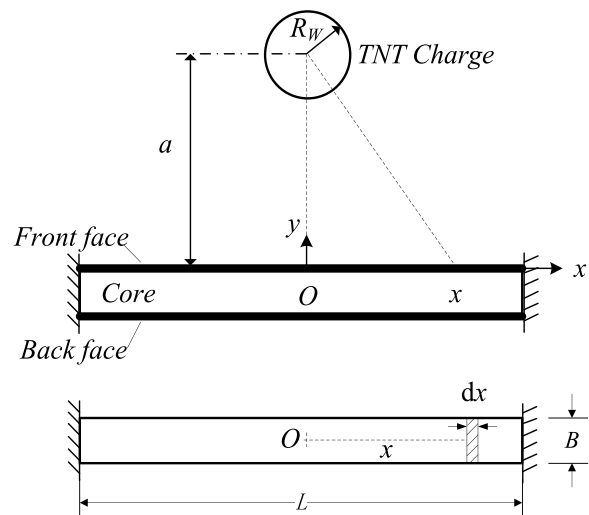
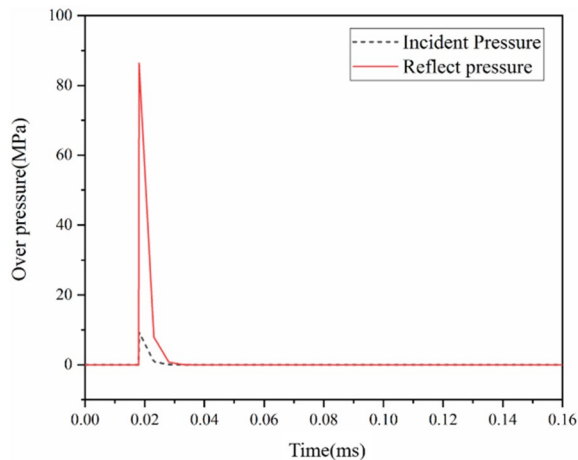


Figure 6 Sketch map of the charge condition



**Figure 7** Pressure-time curve of 20gTNT charge blast at 80 mm standoff distance

as the ratio of the total energy absorption ( $W$ ) to the mass of structure ( $M$ ), as follows:

$$SEA = \frac{W}{M}. \tag{17}$$

Under intensive blast loading, the damage and failure of structure may be an other way for energy dissipation. In present study, we are focus on the dynamic response process and the energy dissipation by the large deformation, so the loading intensity is not very large and the damage and failure of aluminum alloys in FEM can be ignored [68].

### 4.2 Deformation Mode

Under the action of an explosion load, the deformation process of a sandwich structure can be divided into three stages: The over-pressure action stage, core layer compression stage, and overall structure bending deformation stage. Tables 1, 2 and 3 show the typical deformation process of the structure.

In Table 1, it can be seen that the deformation of V10 presented an asymmetric deformation process. The sunken deformation spread to one side, especially for the large core compression stage due to the asymmetric core layer configuration. Compared with the core stiffness of V20 and V25, the core stiffness of V10 was relatively small (as shown in Figure 3), so the core compression stage was longer.

It can be seen from Tables 2 and 3 that at approximately 0.020 ms, the explosion shock wave reached the front face sheet of the structure and interacted with it. The central area of the front panel began to compress the

**Table 2** Deformation process of V20 mode

$t$ (ms)	Core	Beam deformation mode
0		Initial mode
0.020		The initial deformation first occurred at the center area of the front face sheet and core layer
0.040		As the deformation area of the front face sheet expanded, 50% of the first lattice layer of the core was compressed. The second lattice layer of the core and the back face sheet began to deform
0.055		The first lattice layer of the core was densified. The third lattice layer of the core began to deform
0.080		The compression deformation process of the core layer was almost terminated
0.345		The deflections of the face sheets reached the maximum values. After that, oscillations were observed until the structure came to rest
1.500		Final deformation mode

core layer. At the same time, the back face sheet did not produce downward displacement, so the core layer began to undergo compression deformation. At approximately 0.040 ms (V20) and 0.036 ms (V25), due to the energy diffusion, 50% of the first lattice layer of the core was compressed with the deformation area of the front face sheet expanding. The second lattice layer of the core and the back face sheet began to deform. At approximately 0.055 ms (V20) and 0.056 ms (V25), the third lattice layer of the core began to deform. The first lattice layer of V20 was densified, but the first lattice layer of V25 was not densified. At approximately 0.080 ms (V20) and 0.076 ms (V25), the deformation of the core layer was finished. After that, the overall bending deformation of the structure dominated. From the ConWep code, the duration time of this blast loading was 0.050 ms [69], so before



0.070 ms, the over-pressure action stage was coupled with the core compression stage. The front and back face sheets reached their maximum deformations at approximately 0.345 ms (V20) and 0.315 ms (V25). The maximum deflections of the front face sheets were 10.802 mm (V20) and 7.565 mm (V25), and the maximum deflections of back face sheets were 5.766 mm (V20) and 4.648 mm (V25). At the end of the deformation process, the structures presented a partial depression of the front face sheet and arched deformation pattern of the back face sheet.

### 4.3 Blast Resistance and Energy Absorption

The displacement–time history at the central points of both face sheets and the core compression strains of







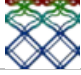







three types of beams are illustrated in Figure 8. The normalized deflection ( $\bar{w} = w/L$ ) of the front face started at the normalized time ( $\bar{t} = t/L\sqrt{\rho_f/\sigma_{fy}}$ ) of 0.015, and then it increased gradually and reached a peak at approximate normalized times of 0.727 ms (V10), 0.341 ms (V20), and 0.312 ms (V25). After that, oscillations were observed until the structure came to rest. The deflection of the back face increased at a slower pace than the rate at which the front face deformed. Core crushing commenced at  $\bar{t} = 0.015$ , and the curves increased sharply until about  $\bar{t} = 0.223$  (V10),  $\bar{t} = 0.074$  (V20), and  $\bar{t} = 0.060$  (V25). Then, the speed of crushing became much slower, and the permanent core compression strains of V10, V20, and V25 were 0.434, 0.166, and 0.096, respectively.

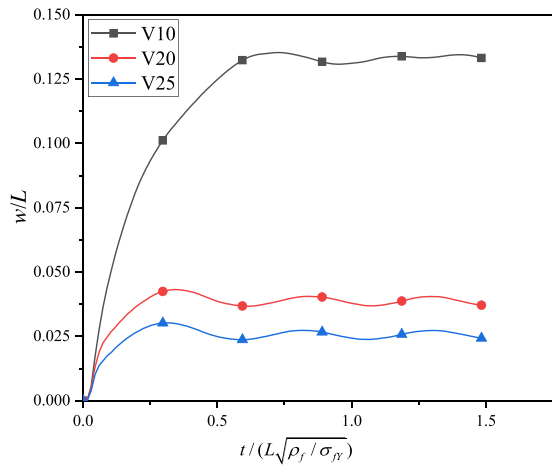
Figure 9 compares the energy absorption histories and SEAs of the three sandwich structures. It can be seen from Figure 9(a) that when the normalized time  $\bar{t} < 0.25$ , the slope of the energy–time curve of V20 was larger than those for the other two, which indicated that the energy dissipation rate of V20 was the best. From Figure 9(b), the SEA of V10 was the largest, reaching 2487 kJ/kg, while that of V20 was 1379 kJ/kg, and that of V25 was the smallest, reaching 806 kJ/kg. Therefore, the energy absorption capacity of V10 was the best. However, due to the large deformation deflection of the back face sheet, V10 is not the best choice for a blast-resistant structure. Compared with V25, V20 had lower mass and better energy absorption, and the back face sheet deformation deflection was close to that of V25.

To rule out the influence of the structural mass, the deflections and SEAs of the beams with the same mass per unit area are shown in Figure 10. The front and back face sheets of V10 and V20 were thickened to 3.24 and 1.63 mm to obtain V10-F and V20-F, respectively. The overall weights of the two structures were the same as that of V25, which was approximately 186 g, and the mass per unit area was 2.48 g/cm<sup>2</sup>. The configuration of each beam is listed in Table 4. The other geometric and material parameters were the same as those in Section 3.

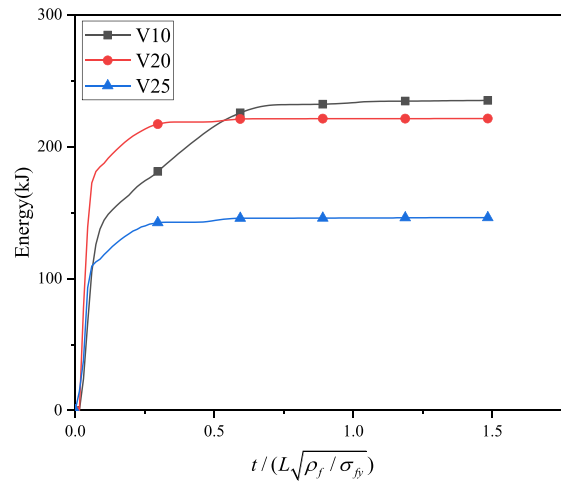
The final deformation mode and transverse displacement field are shown in Figure 10. Due to the asymmetric core layer configuration of V10-F, the structure presented an asymmetric deformation mode accompanied by a large deformation of the core layer. It is evident that with the thickness of the face sheets increasing, the core compression and back face sheet deflection decreased. Because the inclined core web of the V10-F was apt to lose stability, the core compression amount was also larger than those of the others, although the face sheets were thickened.

**Table 3** Deformation process of V25 mode

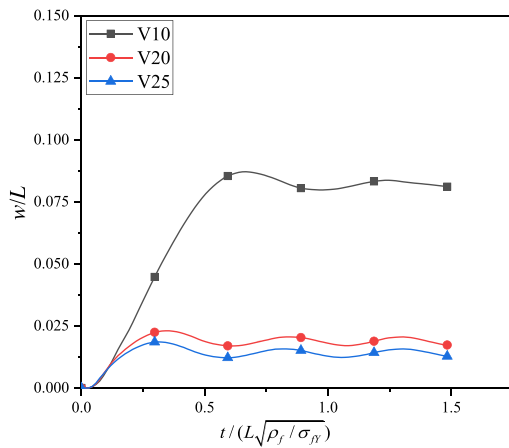
t (ms)	Core	Beam deformation mode
0.000		Initial mode 
0.020		The initial deformation first occurred at the center area of the front face sheet and core layer 
0.036		With the deformation area of the front face sheet expanding, 50% of the first lattice layer of the core was compressed. The second lattice layer of the core and the back face sheet began to deform 
0.056		The third lattice layer of the core began to deform. However, the first lattice layers of the core were not densified 
0.076		The compression deformation process of the core layer was almost terminated 
0.315		The deflections of the face sheets reached the maximum values. After that, oscillations were observed until the structure came to rest 
1.500		Final deformation mode 



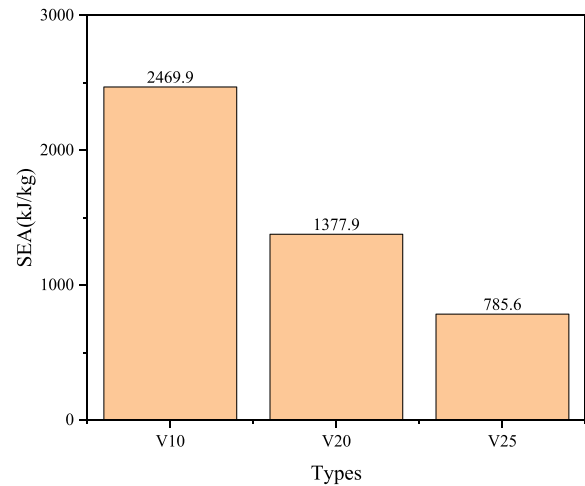
(a) Front face sheet



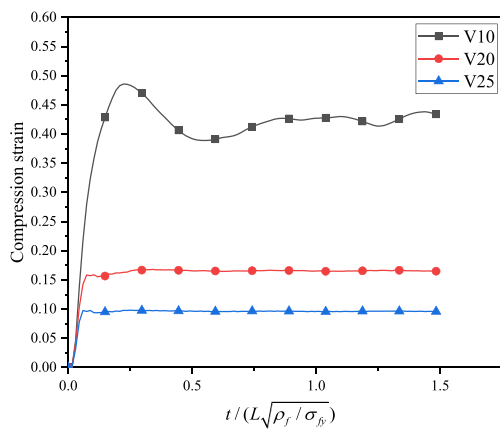
(a) Energy absorption



(b) Back face sheet



(b) SEA



(c) Core layer

**Figure 8** Face sheet displacement and core compression history at the center point of beams

**Figure 9** Energy absorption history and SEA of the sandwich beams with different core volume fraction

From Figure 11(a), it can be seen that when the overall mass of the structure was the same, the maximum deflection gap was evident. Under the same TNT charge conditions, V20-F had the minimum deflection. The maximum deflection of V10-F was much higher than those of the other two groups; it was 136.49% higher than that of V20-F. The maximum deflection of V25 was 34.93% higher than that of V20-F. From the perspective of residual deflection, the residual deflection of V10-F was 46.75% higher than that of V20-F, and the residual deflection of V25 was 41.64% higher than that of V20-F.

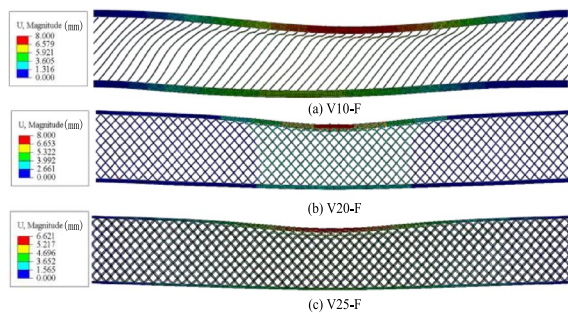


**Figure 10** Final deformation mode and transverse displacement field of the sandwich beams with same mass per unit area

The specific energy absorption amounts of the three structures are shown in Figure 11(b). When the overall mass of the structure was the same, the energy absorption of V20-F was the largest, reaching 1301.5 kJ/kg, which was approximately 1.37 times that of V10-F and 1.66 times that of V25. By comparing the specific energy absorption amounts of V10 and V10-E, it can be found that the thickened face sheet led to a reduction of 61.5% in the energy absorption capacity of the structure. This was apparently because the deflection and the core compression decreased as the thickness of the face sheets increased, which greatly reduced the energy absorption efficiency. However, the SEA of V20-F decreased slightly, which was just reduced by 5.5%. The energy absorption ratios ( $\kappa$ ) of the sandwich beams are shown in Figure 11(c). The energy absorbed by the front face sheet increased from 8% to 17%, the energy absorbed by the back face sheet decreased from 8% to 4%, and the energy absorbed by the core layer decreased from 84% to 79% when the thickness of the face sheet was thickened to 1.63 mm in mode V20-F. This showed that for the same mass per unit area, the structure of V20-F was the best blast resistance configuration, the structure of V25 was in the middle, and the structure of V10-F was the worst. It was demonstrated that only the appropriate combination of the face sheet thickness and core volume fraction could provide better impact resistance and energy absorption characteristics.

#### 4.4 Effects of Filter Radius $r_{\min}$

The final micro-structures and effective elasticity matrices of PBCs of 20% volume fraction with different filter radii  $r_{\min}$  are shown in Figure 12. Their shear elasticity moduli are compared in Figure 13. The shear elasticity modulus decreased with  $r_{\min}$  increasing.

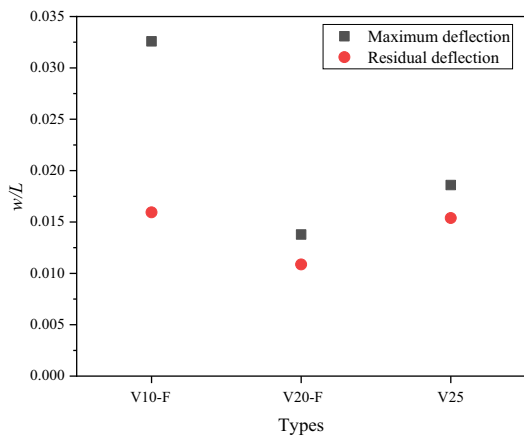
The deflections of the back face sheets ( $W=20$  g,  $a=80$  mm) are compared in Figure 14. Under the same TNT charge conditions, three types of beams ( $r_{\min}=2, 3,$  and  $4$ ) presented similar normalized maximum and residual deflections, which were 0.023 and 0.020, respectively. This demonstrated that the filter radius had little effect on the deformation of the sandwich beam.

The velocities of the back face sheets are compared in Figure 15. Under the same TNT charge condition, the velocity–time curves were almost superimposed before  $\bar{t} = 1.0$ . The beam with  $r_{\min} = 2$  had the maximum peak velocity, which was approximately 39.54 m/s. The beam with  $r_{\min} = 3$  had the minimum peak velocity, which was approximately 37.48 m/s. After 1 ms, there were few differences between the three curves. The beam with  $r_{\min} = 4$  had the highest vibrational frequency, and the beam with  $r_{\min} = 2$  had the lowest vibrational frequency. This demonstrated that increasing the filter radius could slightly improve the bending stiffness of a sandwich beam.

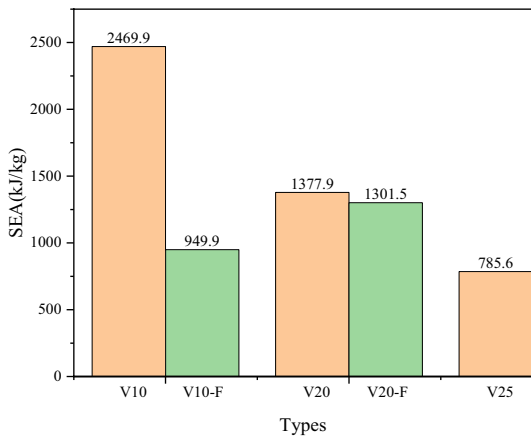
With the change in the PBC aspect ratio, the PBCs showed different topological structures. Because the sandwich core structure was composed of a periodic combination of PBCs, the different topological structures of the PBC were considered to have evolved from the basic configuration type-(a), as shown in Figure 16(a). There are three methods of evolution. The first is to change the angle between the adjacent bars, to make it easier to compress and absorb more energy, such as types-(c) and -(f), as shown in Figure 16(c), (f). This can be regarded as the new configuration obtained when the angles of the bars in type-(a) were changed. The second is to further form holes in the bars so that they can dissipate more energy when deformed, such as type-(b), as shown in Figure 16(b). This can be regarded as further holing of the bars of type-(a). The third is to combine the

**Table 4** Configurations of the beams with the same mass per unit area

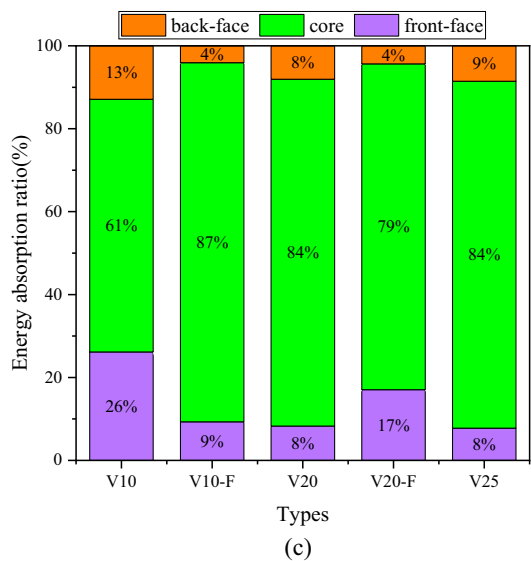
Mode	Face sheets		Core layer (g)	Total mass (g)	Mass per unit area (g/cm <sup>2</sup> )
	Thickness (mm)	Mass (g)			
V10-F	3.24	65.61	54.67	185.90	2.48
V20-F	1.63	33.01	120.10	186.12	
V25	1.00	20.25	145.56	186.06	



(a)



(b)



(c)

Figure 11 (a) Back face sheet deflection, (b) SEA and (c) energy absorption ratio of the beams with same mass per unit area

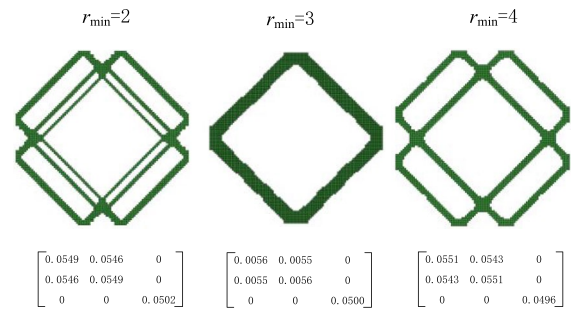


Figure 12 Micro-structures and effective elasticity matrix of PBC with different filter radius  $r_{min}$

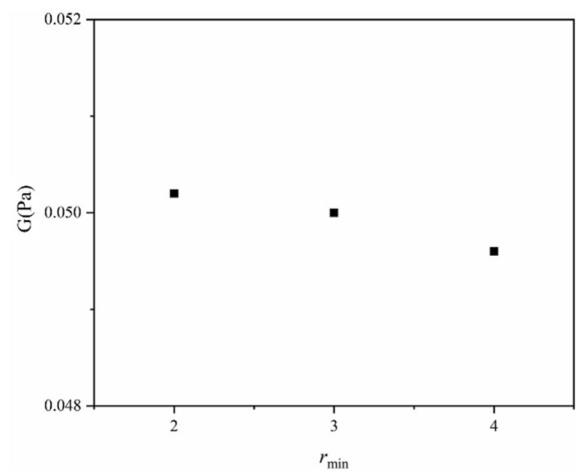


Figure 13 Shear elasticity modulus of PBC with different filter radius  $r_{min}$

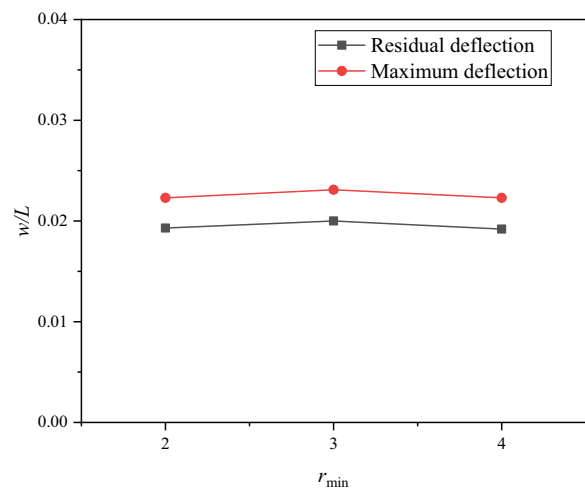
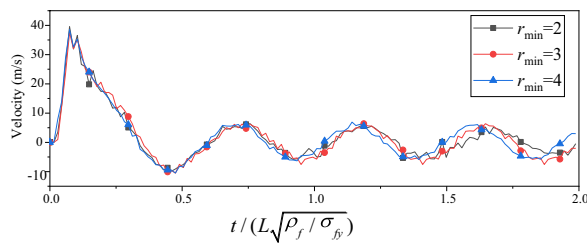
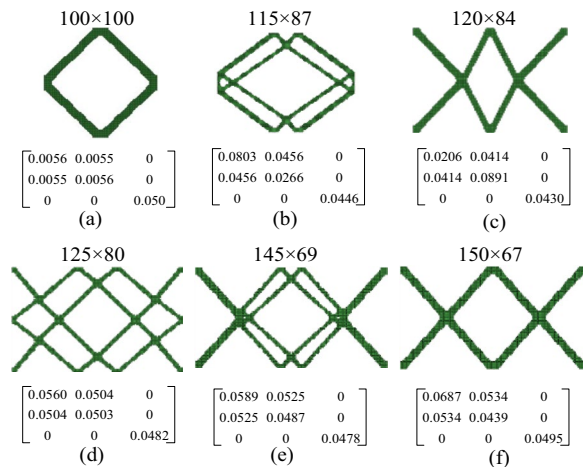


Figure 14 Back face sheet deflection of sandwich beams with different filter radius ( $W = 20$  g,  $a = 80$  mm)



**Figure 15** Back face sheet velocity of sandwich beams with different filter radius ( $W = 20$  g,  $a = 80$  mm)



**Figure 16** Micro-structures and effective elasticity matrix of PBC with different aspect ratio

first two methods, such as types-(d) and -(e), as shown in Figure 16(d), (e).

Due to the different lengths and widths of the PBC, the corresponding sandwich beam dimensions ( $L \times H$ ) could not be the same. Table 5 shows the specific size parameters of the structure. The mass of the core layer ( $M_C$ ) was  $97 \text{ g} \pm 3\%$ . The length and width of the beam were  $253 \text{ mm} \pm 1\%$  and  $22 \text{ mm} \pm 9\%$ , respectively.

Figure 17 shows that the shear moduli of the six types of PBCs were between 0.043 and 0.050. Thus, changing the number of transverse and longitudinal elements of the PBC had little effect on its shear modulus. The back face sheet velocities of the six types of sandwich beams ( $W = 20 \text{ g}$ ,  $a = 80 \text{ mm}$ ) are compared in Figure 18. The

vibrational frequencies of the sandwich beam with type-(a) and type-(d) configurations of the core layer were slightly higher than those of the others, which demonstrated that the aspect ratio of the PBC also had some effect on the bending stiffnesses of the structures.

Figure 19 shows the maximum back face sheet deflection under different TNT charge conditions. The sandwich beam with the type-(d) configuration core layer had the best blast resistance. The sandwich beam with the type-(a) configuration core layer was in second place. The sandwich beam with the type-(c) configuration core layer had the worst blast resistance. The deflection of the sandwich beam with the type-(c) configuration core layer was approximately 1.29 times that of the sandwich beam with the type-(d) configuration core layer under the 20 g TNT charge condition. With the TNT charge increased, the blast resistance advantage of the type-(d) configuration was more distinct.

It can be seen from the above results that although the optimal structure may not be always obtained by selecting an initial square design domain in the topology optimization of the core layer, relatively satisfactory results could be obtained. Changing the aspect ratio of the design domain arbitrarily may lead to worse results. More detailed studies are necessary if further optimization is to be achieved.

Although the configurations of types-(a), -(c), and -(f) had the most similar shapes (as shown in Figure 16), but the deflections of the sandwich beam with type-(a) and type-(f) core layers were smaller than that of the sandwich beam with the type-(c) core layer. Figure 20 shows the deformation modes of the two sandwich beams with the type-(c) and type-(f) core layers. The deformation mode of the sandwich beam with the type-(a) core layer is shown in Table 2. Because the center angle of the type-(c) configuration was too small, at approximately  $57^\circ$ , it was difficult to compress. This configuration was defined as Type II [70] for energy absorption structures and is disadvantageous for energy dissipation under impact and blast conditions. Compared with the type-(c) configuration, the center angles of the type-(a) and type-(f) configurations were approximately  $90^\circ$ , and thus, they were easily compressed. Thus, the energy absorption and core compression capacity of type-(a) and -(f) were much better than that of type-(c), as shown in Figure 21.

**Table 5** Configuration parameters of sandwich beams with different aspect ratios of PBCs

Type	(a)	(b)	(c)	(d)	(e)	(f)
ELEs	100 × 100	115 × 87	120 × 84	125 × 80	145 × 69	150 × 67
$L \times H$ (mm <sup>2</sup> )	250 × 22	253 × 21.75	252 × 21	250 × 24	253.75 × 20.7	255 × 20.1
$M_C$ (g)	100.09	95.78	96.36	97.88	97.82	94.93

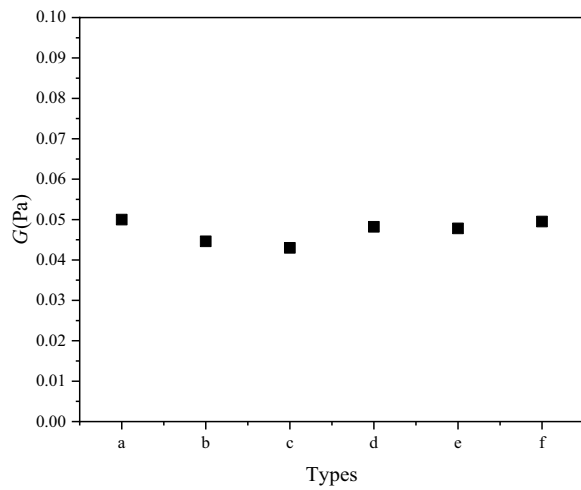


**Figure 17** Shear elasticity modulus of PBC with different aspect ratio

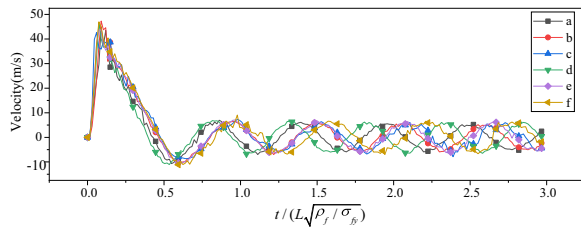


**Figure 18** Back face sheet velocity of sandwich beams with different filter radius ( $W = 20$  g,  $a = 80$  mm)

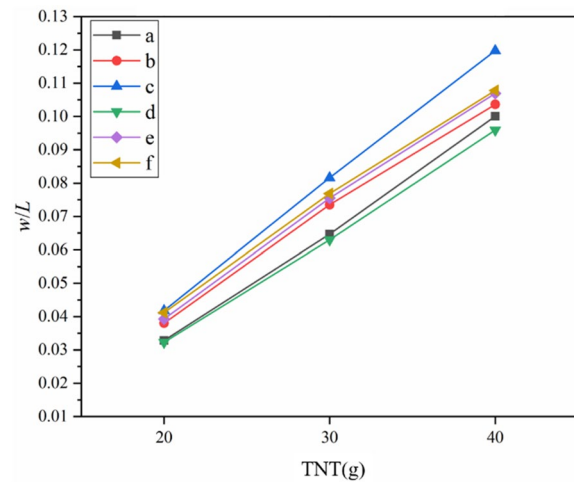
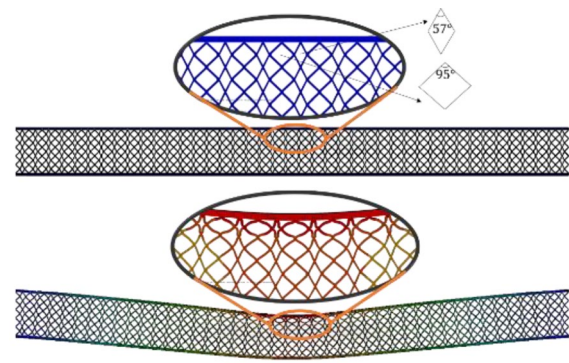
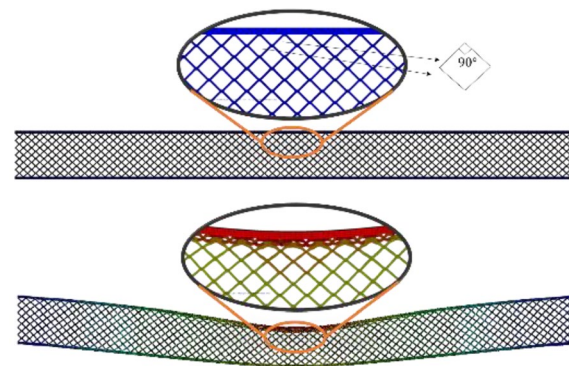


**Figure 19** Normalized maximum deflection of the six types of sandwich beams under different TNT charge ( $a = 80$  mm)

Figure 21 shows the core compression strains and energy absorption capacities of the six types of sandwich beams under the same charge condition of  $W=20$  g and  $a=80$  mm. By comparing type-(a) with type-(b), it



(a) Type-(c) configuration core



(b) Type-(f) configuration core

**Figure 20** Deformation mode of the sandwich beams with type-(c) and type-(f) configuration core

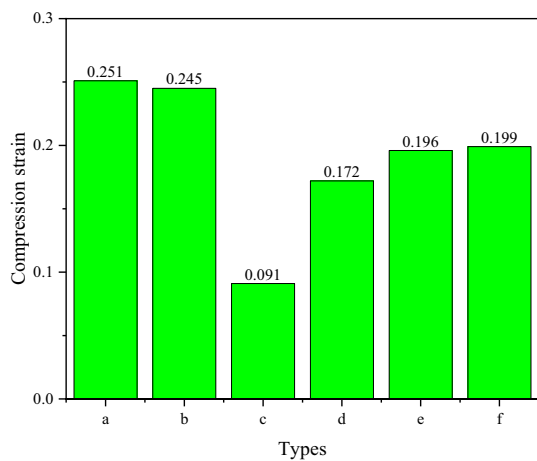
can be seen that forming holes in the bars could improve the energy absorption. By comparing type-(c) with type-(f), it can be seen that increasing the angle between the adjacent bars could increase the core compression and improve the energy absorption. However, not all three methods could improve the energy absorption capacity of the structure. The core compression strains and energy absorption capacities of the structures were significantly affected by the aspect ratio of the PBC.

### 5 Conclusions

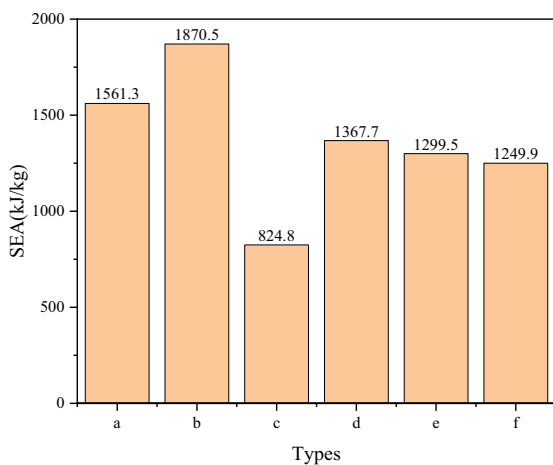
In the present study, the BESO method was employed to optimize the core layer with a periodic base cell and extreme shear stiffness. The dynamic responses and energy absorption amounts of sandwich beams with optimal core layers were analyzed by the finite element method. The effects of the volume fraction, filter radius, and initial PBC aspect ratio on the micro-topologies of

the cores and the dynamic response processes, core compression strains, and energy absorption capacities of the sandwich beams with optimal core layers under blast impact loading were discussed in detail.

Under blast loading, the sandwich beams presented typical three-stage response: The over-pressure action stage, core compression stage, and global bending deformation stage. From the deformation process, it was demonstrated that the over-pressure action stage was coupled with the core compression stage. Under the same loading and same mass per unit area, the sandwich beam with a 20% volume fraction core layer had the best blast resistance.



(a) Core compression



(b) Energy absorption capacity

**Figure 21** Core compression and energy absorption capacity of the six types of sandwich beams

With the filter radius changing, the topology of the PBC presented some different configurations, but the shear stiffness and blast resistances of the sandwich beams were similar, and the bending stiffness of the sandwich beams were slightly improved. Upon changing the initial PBC aspect ratio, there are three ways for the PBC evolution: The first is to change the angle between the adjacent bars, the second is to further form holes in the bars, and the third is to combine the first two methods. Although a much bigger angle between the adjacent bars and more holes in the bars can improve the energy absorption amounts and core compression capacities of the structures, not all three methods can improve the energy absorption capacities of the structures, and changing the aspect ratio of the design domain arbitrarily may lead to worse results.

#### Acknowledgements

It is a great pleasure to thank LetPub ([www.letpub.com](http://www.letpub.com)) for its linguistic assistance and Prof. Xiaodong Huang in Swinburne University of Technology for his suggestions during the preparation of this manuscript.

#### Authors' Contributions

ZW was in charge of the whole trial; SL wrote the manuscript; YL assisted with sampling and laboratory analyses. XM wrote the review. JF was in charge of writing and editing. ZL was in charge of validation. All authors read and approved the final manuscript.

#### Funding

Supported by National Natural Science Foundation of China (Grant Nos. 12072219, 12202303, 12272254), Shanxi Provincial Excellent Talents Science and Technology Innovation Project of China (Grant No. 201805D211033).

#### Data availability

Data will be made available on request.

#### Declarations

#### Competing Interests

The authors declare no competing financial interests.

Received: 1 November 2022 Revised: 22 May 2024 Accepted: 29 May 2024

Published online: 21 August 2024

#### References

- [1] H Liu, H Liu, J Yang. Clamped sandwich beams with thick weak cores from central impact: A theoretical study. *Composite Structures*, 2017, 169: 21–28.
- [2] W Hou, F Zhu, G Lu, et al. Ballistic impact experiments of metallic sandwich panels with aluminium foam core. *International Journal of Impact Engineering*, 2010, 37(10): 1045–1055.
- [3] V Rizov, A Shipsha, D Zenkert. Indentation study of foam core sandwich composite panels. *Composite Structures*, 2005, 69(1): 95–102.
- [4] F Zhu, Z Wang, G Lu, et al. Some theoretical considerations on the dynamic response of sandwich structures under impulsive loading. *International Journal of Impact Engineering*, 2010, 37(6): 625–637.
- [5] F Zhu, L Zhao, G Lu, et al. A numerical simulation of the blast impact of square metallic sandwich panels. *International Journal of Impact Engineering*, 2009, 36(5): 687–699.
- [6] Z Wang. Recent advances in novel metallic honeycomb structure. *Composites. Part B, Engineering*, 2019, 166: 731–741.

- [7] Z Wang, X Wang, K Liu, et al. Crashworthiness index of honeycomb sandwich structures under low-speed oblique impact. *International Journal of Mechanical Sciences*, 2021, 208: 106683.
- [8] C Shu, S Zhao, S Hou. Crashworthiness analysis of two-layered corrugated sandwich panels under crushing loading. *Thin-Walled Structures*, 2018, 133: 42–51.
- [9] W Chang, E Ventsel, T K rauthammer, et al. Bending behavior of corrugated-core sandwich plates. *Composite Structures*, 2005, 70(1): 81–89.
- [10] N Wicks, J W Hutchinson. Performance of sandwich plates with truss cores. *Mechanics of Materials*, 2004, 36(8): 739–751.
- [11] A G Evans, J W Hutchinson, N AFleck, et al. The topological design of multifunctional cellular metals. *Progress in Materials Science*, 2001, 46(3): 309–327.
- [12] V S Deshpande, N A Fleck. Effective properties of the octet-truss lattice material. *Journal of the Mechanics and Physics of Solids*, 2001(49): 687–705.
- [13] Z Wang, Y Zhou, X Wang, et al. Compression behavior of strut-reinforced hierarchical lattice-Experiment and simulation. *International Journal of Mechanical Sciences*, 2021, 210: 106749.
- [14] S H Yoo, S H Chang. An experimental study on energy absorbing structures made of fabric composites. *Composite Structures*, 2008, 86(1): 211–219.
- [15] T Gao, K Liu, X Wang, et al. Elastic mechanical property hybridization of configuration-varying TPMS with geometric continuity. *Materials & Design*, 2022, 221: 110995.
- [16] C Li, H Shen, H Wang. Nonlinear bending of sandwich beams with functionally graded negative Poisson's ratio honeycomb core. *Composite Structures*, 2019, 212: 317–325.
- [17] W Lv, D Li, L Dong. Study on blast resistance of a composite sandwich panel with isotropic foam core with negative Poisson's ratio. *International Journal of Mechanical Sciences*, 2021, 191.
- [18] L Shen, X Wang, Z Li, et al. Elastic properties of an additive manufactured three-dimensional vertex-based hierarchical re-entrant structure. *Materials & Design*, 2022, 216: 110527.
- [19] L Shen, Z Wang, X Wang, et al. Negative Poisson's ratio and effective Young's modulus of a vertex-based hierarchical re-entrant honeycomb structure. *International Journal of Mechanical Sciences*, 2021, 206: 106611.
- [20] Z Wang, Z Guo, Z Li, et al. Coupling and scaling effect for low-frequency broadband sound absorption via vertex-based hierarchy. *Applied Physics Letters*, 2021, 119(17): 171903.
- [21] Z Li, X Li, Z Wang, et al. Multifunctional sound-absorbing and mechanical metamaterials via a decoupled mechanism design approach. *Materials Horizons*, 2023, 10(1): 75–87.
- [22] Z Li, W Zhai, X Li, et al. Additively manufactured dual-functional metamaterials with customisable mechanical and sound-absorbing properties. *Virtual and Physical Prototyping*, 2022, 17(4): 864–880.
- [23] Z Wang, Z Guo, Z Li, et al. Design, manufacture, and characterisation of hierarchical metamaterials for simultaneous ultra-broadband sound-absorbing and superior mechanical performance. *Virtual and Physical Prototyping*, 2023, 18(1).
- [24] K Zeng, Z Li, Z Guo, et al. Acoustic metamaterial for highly efficient low-frequency impedance modulation by extensible design. *Extreme Mechanics Letters*, 2022, 56: 101855.
- [25] Z Li, Z Wang, Z Guo, et al. Ultra-broadband sound absorption of a hierarchical acoustic metamaterial at high temperatures. *Applied Physics Letters*, 2021, 118(16): 161903.
- [26] S N ikbakt, S Kamarian, M Shakeri . A review on optimization of composite structures Part I: Laminated composites. *Composite Structures*, 2018, 195: 158–185.
- [27] S Nikbakht, S Kamarian, M Shakeri. A review on optimization of composite structures Part II: Functionally graded materials. *Composite Structures*, 2019, 214: 83–102.
- [28] Y Zhang, M Xiao, X Zhang, et al. Topological design of sandwich structures with graded cellular cores by multiscale optimization. *Computer Methods in Applied Mechanics and Engineering*, 2020, 361: 112749.
- [29] M P Bendsøe. Optimal shape design as a material distribution problem. *Structural Optimization*, 1989, 1(4): 193–202.
- [30] Y M Xie, G P Steven. A simple evolutionary procedure for structural optimizati. *Computers & Structures*, 1993, 49(5): 885–896.
- [31] X Huang, Y M Xie. Convergent and mesh-independent solutions for the bi-directional evolutionary structural optimization method. *Finite Elements in Analysis and Design*, 2007, 43(14): 1039–1049.
- [32] L Xia, Q Xia, X Huang, et al. Bi-directional evolutionary structural optimization on advanced structures and materials: A comprehensive review. *Archives of Computational Methods in Engineering*, 2018, 25(2): 437–478.
- [33] X Guo, W Zhang, J Zhang, et al. Explicit structural topology optimization based on moving morphable components (MMC) with curved skeletons. *Computer Methods in Applied Mechanics and Engineering*, 2016, 310: 711–748.
- [34] Y Zhou, W Zhang, J Zhu, et al. Feature-driven topology optimization method with signed distance function. *Computer Methods in Applied Mechanics and Engineering*, 2016, 310: 1–32.
- [35] W Zhang, Y Zhou, J Zhu. A comprehensive study of feature definitions with solids and voids for topology optimization. *Computer Methods in Applied Mechanics and Engineering*, 2017, 325: 289–313.
- [36] M Y Wang , X Wang, D Guo. A level set method for structural topology optimization. *Computer Methods in Applied Mechanics and Engineering*, 2003, 192(1): 227–246.
- [37] H Li, Z Luo, L Gao, et al. Topology optimization for functionally graded cellular composites with metamaterials by level sets. *Computer Methods in Applied Mechanics and Engineering*, 2018, 328: 340–364.
- [38] H Ye, Z Dai, W Wang, et al. ICM method for topology optimization of multimaterial continuum structure with displacement constraint. *Acta Mechanica Sinica*, 2019, 35(3): 552–562.
- [39] J Rong, L Yu, X Rong, et al. A novel displacement constrained optimization approach for black and white structural topology designs under multiple load cases. *Structural and Multidisciplinary Optimization*, 2017, 56(4): 865–884.
- [40] G Gupta, J Tan, C Conner. Me design and free form fabrication of compliant cellular materials with graded stiffness. *Solid Free Form Fabrication Symposium*, Austin, TX(US), 2006.
- [41] X Huang, A Radman, Y M Xie. Topological design of microstructures of cellular materials for maximum bulk or shear modulus. *Computational Materials Science*, 2011, 50(6): 1861–1870.
- [42] E Andreassen, C S Andreassen. How to determine composite material properties using numerical homogenization. *Computational Materials Science*, 2014, 83: 488–495.
- [43] L Liu, J Yan, G Cheng. Optimum structure with homogeneous optimum truss-like material. *Computers & Structures*, 2008, 86(13): 1417–1425.
- [44] S Sun, W Zhang, K Qiu, et al. Integrated topology optimization and scale effect analysis of cyclic symmetry sandwich structures. *Chinese Journal of Theoretical and Applied Mechanics*, 2007, 39(6): 788–795. (in Chinese)
- [45] T Strekot, H Jopek, B T Maruszewski, et al. Computational analysis of sandwich-structured composites with an auxetic phase. *Physica Status Solidi (b)*, 2014, 251(2): 354–366.
- [46] K Long, D Han, X Gu. Concurrent topology optimization of composite macrostructure and microstructure constructed by constituent phases of distinct Poisson's ratios for maximum frequency. *Computational Materials Science*, 2017, 129: 194–201.
- [47] X Huang, Y M Xie, G Lu. Topology optimization of energy-absorbing structures. *International Journal of Crashworthiness*, 2007, 12(6): 663–675.
- [48] F Duddeck, S Hunkeler, P Lozano. Topology optimization for crashworthiness of thin-walled structures under axial impact using hybrid cellular automata. *Structural&Multidisciplinary Optimization*, 2016: 1–14.
- [49] N M Patel, B S Kang, J E Renaud. Crashworthiness design using topology optimization. *Dissertations&Theses-Gradworks*, 2009, 6(131): 277–283.
- [50] A Tovar, N M Patel, A K Kaushik. Hybrid Cellular Automata: A biologically-inspired structural optimization technique. *Proceedings of the Tenth AIAA/ISSMO Symposium on Multidisciplinary Analysis and Optimization*, Albany, NY, 2004.
- [51] G Park. Technical overview of the equivalent static loads method for nonlinear static response structural optimization. *Structural and Multidisciplinary Optimization*, 2011, 43(3): 319–337.
- [52] A Kaushik, A Ramani. Topology optimization for nonlinear dynamic problems: Considerations for automotive crashworthiness. *Engineering Optimization*, 2014, 4(46): 487–502.
- [53] K Yan. *Structural optimization method of sturce subject to impact loads*. Dalian: Dalian University of Technology, 2016.



- [54] K Yan, G Cheng. A hybrid approach to structural topology optimization of vehicle for crashworthiness. *APCOM&ISCM-2013*, Singapore, 2013.
- [55] L Jing, X Su, L Zhao. The dynamic compressive behavior and constitutive modeling of D1 railway wheel steel over a wide range of strain rates and temperatures. *Results in Physics*, 2017, 7: 1452–1461.
- [56] L Jing, X Su, C Feng, et al. Strain-rate dependent tensile behavior of railway wheel/rail steels with equivalent fatigue damage: Experiment and constitutive modeling. *Engineering Fracture Mechanics*, 2022, 275: 108839.
- [57] Z Sun, D Li, W Zhang, et al. Topological optimization of biomimetic sandwich structures with hybrid core and CFRP face sheets. *Composites Science and Technology*, 2017, 142: 79–90.
- [58] L Xia, P Breitkopf. Design of materials using topology optimization and energy-based homogenization approach in Matlab. *Structural and Multi-disciplinary Optimization*, 2015, 52(6): 1229–1241.
- [59] B Hassani, B Hinton. A review of homogenization and topology optimization III-topology optimization using optimality criteria. *Computers and Structures*, 1998, 69(6): 739–759.
- [60] X Huang, Y M Xie. *Evolutionary topology optimization of continuum structures: Methods and applications*. Chichester: John Wiley & Sons, 2010.
- [61] J Henrych. *The dynamics of explosion and its use*. Amsterdam Oxford New York: Elsevier Scientific Publishing Company, 1979.
- [62] S Li, G Lu, Z Wang, et al. Finite element simulation of metallic cylindrical sandwich shells with graded aluminum tubular cores subjected to internal blast loading. *International Journal of Mechanical Sciences*, 2015, 96–97: 1–12.
- [63] S Li, Z Wang, G Wu, et al. Dynamic response of sandwich spherical shell with graded metallic foam cores subjected to blast loading. *Composites Part A Applied Sciences and Manufacturing*, 2014, 56: 262–271.
- [64] G N Nurick, G S Langdon, Y Chi, et al. Behaviour of sandwich panels subjected to intense air blast-Part 1: Experiments. *Composite Structures*, 2009, 91(4): 433–441.
- [65] X Li, X Ma, S Li, et al. Deformation and failure of a novel fiber-metal hybrid lamina composite under quasi-static and impact loading. *Composites Science and Technology*, 2021, 216: 109067.
- [66] X Li, R Xu, X Zhang, et al. Inner blast response of fiber reinforced aluminum tubes. *International Journal of Impact Engineering*, 2023, 172: 104416.
- [67] S Li, X Li, Z Wang, et al. Sandwich panels with layered graded aluminum honeycomb cores under blast loading. *Composite Structures*, 2017, 173: 242–254.
- [68] D Karagiozova, G N Nurick, G S Langdon. Behaviour of sandwich panels subject to intense air blasts-Part 2: Numerical simulation. *Composite Structures*, 2009, 91(4): 442–450.
- [69] CONWEP. Conventional weapons effects program, version 2.00, 1991.
- [70] G Lu, T X Yu. *Energy absorption of structures and materials*. Abington: Woodhead Publishing Limited, 2003.

**Shiqiang Li** born in 1986, is currently a associate professor at *Institute of Applied Mechanics, Taiyuan University of Technology, China*.

**Yuwei Li** born in 1999, is currently a master candidate at *Taiyuan University of Technology*. Her research interests include dynamic response of structure and structure optimization.

**Xiaomin Ma** born in 1988, is currently a lecturer at *Institute of Applied Mechanics, Taiyuan University of Technology, China*.

**Jianguang Fang** born in 1987, is currently a lecturer at *University of Technology Sydney, Australia*.

**Zhifang Liu** born in 1971, is currently a professor at *Institute of Applied Mechanics, Taiyuan University of Technology, China*.

**Zhihua Wang** born in 1977, is currently a professor at *Institute of Applied Mechanics, Taiyuan University of Technology, China*.